Thermal Performance Optimization Study of Two Types of Side Cooling Plates for 280Ah Battery Modules

Yujie CHEN [a,], Lihua CAI [a,b], Dianxu RUAN [c], Haifeng FANG [a,b], Ziwei ZHANG[a]*

[a] College of Mechanical Engineering, Jiangsu University of Science and Technology, Zhenjiang, 212100, Jiangsu, China

[b] Suzhou Institute of Technology, Jiangsu University of Science and Technology, Suzhou, 215600 Jiangsu, China

[c] Shazhou Professional Institute of Technology, Suzhou, 215600, Jiangsu, China

*Corresponding Author Email: 1903382479@qq.com

Energy storage battery packs generate a significant amount of heat during operation, affecting battery performance and lifespan, and potentially leading to safety risks. Consequently, the design of efficient battery cooling plates is essential for maintaining the performance of energy-storage battery packs. This study performs a comparative investigation of the cooling efficacy of ECP versus MCP. We created and enhanced three model sets for the two types of cooling plates. The findings indicate that lowering the coolant inlet temperature reduces the peak temperature of the batteries in both cooling plate types, while simultaneously increasing the maximum temperature differential. Augmenting the coolant flow rate concurrently diminishes both the peak battery temperature and the maximum temperature differential. From the three models of ECP, it was found that optimization measures such as reducing channel spacing and increasing the coolant flow distance can improve cooling efficiency. After optimization, the maximum temperature of the A-group model decreased by 1.57°C compared to the initial model. The optimization of the MCP ensured uniform distribution over the battery module while preserving fluid dynamics inside the microchannel configuration. Following optimization, the E-group model demonstrated a temperature decrease of 1.35°C relative to the baseline model, attaining a cooling effect comparable to that of the solid cooling plate. By comparing and analyzing the h_c and Nu of the cooling plate at a m_{in} of 3L/min, it was verified that the optimized MCP heat dissipation performance is consistent with ECP.

Keywords: *$LiFePO_4$ battery, Module cooling, Cooling Plates, Fluent, Simulation model, Battery safety*

1 Introduction

As global warming intensifies, climate challenges have escalated in severity. Energy storage battery systems can optimize the use of renewable energy, diminish dependence on fossil fuel power generation, and decrease greenhouse gas emissions [1]. During the charging and discharging procedures, energy storage batteries produce substantial heat. If this heat is not dispersed efficiently and swiftly, it may result in elevated battery temperatures, thereby diminishing the lifespan of the storage battery system [2-4].

Lithium iron phosphate batteries utilized in energy storage systems generally function best within a temperature range of 20-40°C [5,6]. Moreover, the temperature discrepancies among different batteries must be modest, since excessive or inadequate fluctuation can impact their performance and longevity [7]. Consequently, to guarantee the optimal functioning of the batteries and prolong their longevity, it is imperative to establish a battery thermal management system (BTMS) for efficient heat dissipation[8].

The cooling techniques for lithium iron phosphate batteries are classified into three categories: air cooling [9], liquid cooling [10], and phase-change cooling [11]. Lalan K. Singh et al. [12] employed forced air cooling technology to improve the safe functioning of battery modules; Gang Zhao et al. [13] refined the inlet and outlet of the air cooling system to ensure sufficient cooling for high-density battery modules. Fang et al. [14] employed bottom liquid cooling for battery module temperature regulation, demonstrating that the configuration of the cooling plate channels significantly influences battery temperature. Lin et al. [15] developed a serpentine microchannel cooling plate for lithium batteries, which effectively lowered battery temperature and decreased energy consumption.

Side cooling substantially mitigates the likelihood of thermal runaway. Yansen Zhang et al. [16] studied the effects of side liquid cooling versus side air cooling on the temperature fluctuations of battery modules. The findings indicated that both techniques diminished the temperature disparity of battery modules, and at a power usage of 0.5 watts, the liquid cooling system surpassed the air cooling system. Jiekai Xie et al. [17] employed orthogonal optimization to create and enhance the lateral cooling configuration of battery modules. Their research indicated a strong correlation between cellular temperature regulation and the cooling architecture, illustrating that the incorporation of a diverter can proficiently manage battery temperature and thermal gradients. Kuijie Li et al. [18] employed a multi-objective optimization technique to engineer a lightweight side cooling liquid cooling panel. The mass of the liquid cooling plate was diminished by roughly 59.6%, while the trigger time for thermal runaway events was successfully extended by 15 seconds, illustrating that side cooling effectively mitigates the risk of thermal runaway. Xu et al. [19] modified the ratio of inlet length to height, enabling the unidirectional cooling liquid to maintain the temperature differential of the battery module within 5°C without necessitating a high mass flow rate.

This work categorizes side liquid cooling systems into two types: Entire Cooling Plate (ECP) and Microchannel Cooling Plate (MCP) structures, based on the aforementioned research findings. Three cooling plate models were developed for each category, and thermal simulations were performed for the battery modules. The impact of the inlet temperature on the cooling of the battery module was examined first. The effects of alterations in the cooling plate configuration and the coolant inlet flow rate on the thermal performance of the battery module were examined. A thorough analysis was performed on all preliminarily optimized cooling plates, highlighting the benefits of each kind, so offering a reference for engineering selection.

2 Model Establishment

2.1 Three-Dimensional Model

Individual lithium iron phosphate ($LiFePO_4$) cells exhibit constrained power output; hence, energy storage devices generally amalgamate many cells into a battery pack to fulfil their operating demands. This study focuses on a 1P13S $LiFePO_4$ battery module, employing lateral liquid cooling as the thermal management method. Zhiyang Zou et al. [20] highlighted the necessity of simplifying battery modules in thermal simulations. Accordingly, the simplified model structure used in this study is illustrated in Fig. 1(a). Variations in temperature distribution may arise on the cell surfaces due to disparities in the thermal conductivity of battery materials throughout the x-, y-, and z-directions (particular characteristics detailed in Table 1). We utilize thermal silicone gel between the cells and between the cells and the cooling plate to improve the module's thermal conductivity. Aluminum is widely used in battery module thermal management design due to its excellent thermal conductivity, low cost, and ease of processing. The dimensions of the cooling plate used in this study are shown in Fig. 1(b). The coolant inlet is designed as a rectangular aperture measuring 6×30 mm. The preliminary design of the cooling plate presented in this work, depicted in Fig.1(c), seeks to enhance heat dissipation efficiency to satisfy operational requirements.

Table 1 Parameters of 280Ah LiFePO4 Battery

Parameters	Values
Rated capacity (Ah)	280
Rated voltage (V)	3.2
Internal resistance (mΩ)	≤1.0
Density (kg/m^3)	2110
Specific heat capacity (J/kg/°C)	964
Size of cell (length × width × height) (mm)	174×71×207
Thermal conductivity (X, Y, Z directions) (W/m/°C)	11/9.04/3.56

Previous research has established that side cooling significantly mitigates the likelihood of thermal runaway. Consequently, this work employs lateral cooling to expel heat from the battery module. The influence of various cooling plate configurations on the cooling effect is assessed by altering the inlet temperature and mass flow rate of the cooling plate. Table 2 presents the physical properties of the materials utilized in the battery module.

Table 2 Physical parameters of the material used in battery module structure

Material	Density (kg/m^3)	Thermal conductivity (W/m/°C)	Specific heat (J/kg/°C)
Aluminum	2702	236	903
Heat Conducting Glue	1550	1.6	1.457
Cooling Liquid	1069.4	0.4	3358

The battery module predominantly utilizes liquid cooling for thermal dissipation, with the natural convection heat transfer coefficient of the battery surface air established at 5W/(m²•°C). The initial boundary conditions are established as follows: the ambient temperature outside the battery is 25°C, the coolant inlet temperature is 25°C, the coolant inlet mass flow rate is 3L/min, and the outlet is designated as a pressure outlet (gauge pressure is 0). Simulation analysis is performed on two varieties of side cooling plates: Entire Cooling Plates (ECP) and Microchannel Cooling Plates (MCP), to examine the influence of structure, coolant inlet temperature (T_{in}), and mass flow rate (m_{in}) on the cooling efficacy.

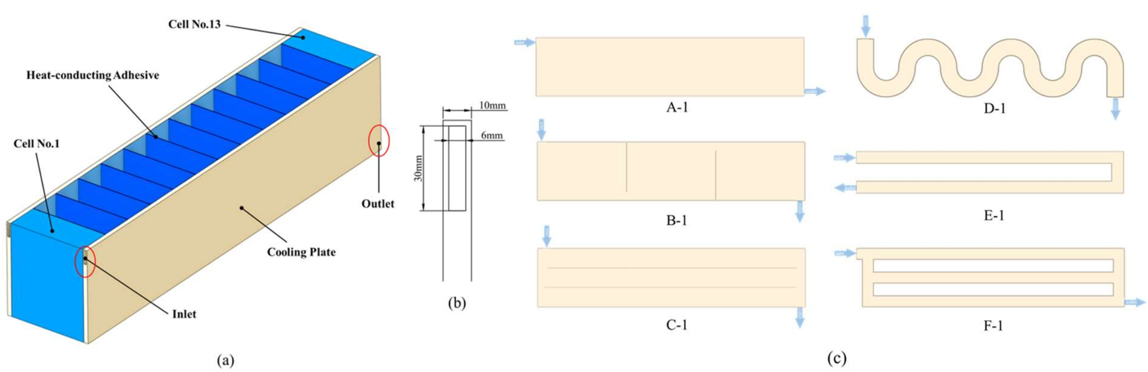

Fig.1. Streamlined representation of the battery module

2.2 Governing Equations

The thermal energy produced by a lithium battery during operation mostly comprises reaction heat Q_r, polarization heat Q_p, Joule heat Q_j, and side reaction heat Q_s [21]. The total heat Q can be calculated using Equation (1):

$$Q = Q_r + Q_p + Q_j + Q_s \tag{1}$$

The reaction heat Q_r can be calculated using Equation (2).

$$Q_r = \frac{nmQI}{MF} \tag{2}$$

In the equation, n represents the total number of batteries; m is the mass of the electrode (g); I is the battery current (A); M is the molar mass (g/mol); F is the Faraday constant.

The Polarization heat Q_p as shown in Equation (3):

$$Q_p = I^2 R_p \tag{3}$$

In the equation, R_p is the polarization internal resistance in ohms (Ω).

Joule heat Q_j can be calculated using the equation (4):

$$Q_j = I^2 R_j \tag{4}$$

In the equation, R_j is the polarization internal resistance in ohms (Ω).

The thermal energy generated by side reactions Qs represents the thermal energy generated by the deterioration of electrode materials and electrolyte during excessive charging and discharging, or at extreme temperatures in lithium-ion batteries. Under standard operational conditions, Qs is typically negligible and therefore overlooked.

Therefore, Equation (1) can be rewritten as

$$Q = Q_r + Q_p + Q_j = \frac{nmQI}{MF} + I^2 R_p + I^2 R_j \tag{5}$$

Studies have shown that the distribution of heat generation in different parts of a lithium-ion battery is strongly correlated with its temperature. When operating within the normal temperature range, the reaction heat contributes only a small proportion [7]. BTMS ensures that the temperature of the lithium-ion battery remains constantly within the optimal working range. Consequently, Equation (5) may be reformulated as:

$$Q = Q_p + Q_j = I^2 R_p + I^2 R_j \tag{6}$$

The Reynolds number Re for liquid flow is:

$$\mathrm{Re} = \frac{\rho \upsilon d}{\mu} \tag{7}$$

where ρ is the fluid density in kg/m³, v is the fluid velocity in m/s, μ is the dynamic viscosity in Pa·s, and d is the characteristic length in meters. The cross-section of the flow channel in this paper is designed as a rectangle, and the characteristic length d can be calculated using Equation (8).

$$d = \frac{2ab}{(a+b)} \tag{8}$$

In the equation, a and b represent the length and width of the rectangle in meters, respectively.

This paper describes a rectangular cross-section measuring 30 mm in length and 6 mm in breadth. With the original boundary conditions, a flow rate of 3L/min results in a Reynolds number of 871.24, which is below 2300.

In engineering applications, it is generally considered that the critical Reynolds number for pipe flow is around 2300. When Re<2300, the fluid is considered to be in laminar flow; when 2300<Re<4000, the fluid is in transitional flow. At this stage, the flow channel structure significantly influences the fluid flow pattern, and in more complex channel structures, the fluid can easily transition to turbulent flow in the pipeline. When Re>4000, the fluid is in a turbulent state. Based on the previous calculation results, the Reynolds number is less than 2300, so this paper adopts a laminar flow model for the simulation calculations.

2.3 CFD Model

During the numerical simulation process, the following assumptions are made to simplify the model [21]:

(1) The coolant is isotropic, incompressible, and its physical properties are independent of temperature;

(2) There is no relative slip between the coolant and the channel walls;

(3) The effects of gravity and viscous dissipation on the flow are neglected.

According to the aforementioned assumptions, the equations for mass conservation, momentum conservation, and energy conservation for the complete microchannel process are as follows:

Mass Conservation Equation：

$$\frac{\partial \rho_f}{\partial t} + \nabla \bullet (\rho_f \vec{v}) = 0 \tag{9}$$

Momentum Conservation Equation：

$$\frac{\partial}{\partial t}\left(\rho_f \vec{v}\right) + \nabla \bullet \left(\rho_f \vec{v}\right) = -\nabla P + \mu_f \nabla^2 \vec{v} \tag{10}$$

Energy Conservation Equation：

$$\frac{\partial}{\partial t}\left(\rho_f c_{p,f} T_f\right) + \nabla \bullet \left(\rho_f c_{p,f} \vec{v} T_f\right) = \nabla \bullet \left(k_f \nabla T_f\right) \tag{11}$$

2.4 Grid Independence Verification

In Fluent software, a finer mesh enhances accuracy but considerably prolongs computation time. Consequently, the quantity of mesh elements significantly influences the outcomes of ensuing numerical simulations [22]. Therefore, to guarantee computational precision while optimizing resource usage, mesh independence validation was conducted. An independent analysis was performed for each model to examine the influence of mesh size on the outcomes of each liquid cooling plate and to assure precision.

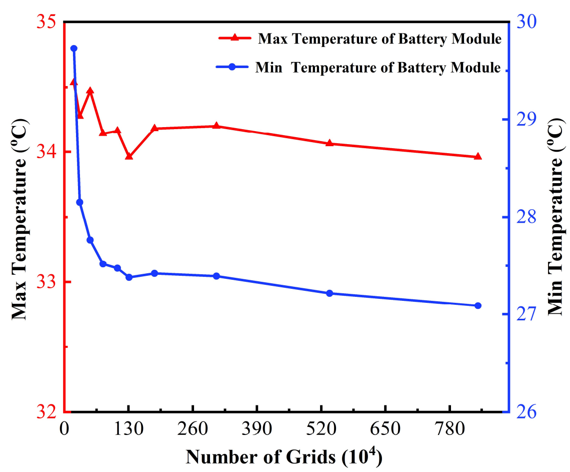

Fig.2. The trend of battery temperature with the change in the number of grids

This study altered the number of mesh elements in the model from 193,072 to 8,371,816. Fig.2 illustrates the impact of mesh quantity on the temperature of the battery module. When the mesh count varied between 1.3 million and 8.37 million, all indicators stabilized, with the average temperature fluctuation remaining within 0.1°C. The numerical alterations were minimal, satisfying the requisite precision. Consequently, a mesh count of 1.3 million was employed for this model, and analogous trends were noted in the mesh independence assessments of other models.

3 Model Validation

3.1Experimental Configuration and Methodology

An experimental system was built to validate the correctness of the numerical simulation results, utilizing the battery module as the study subject, as depicted in Fig.3. This experimental system mainly comprises a power conversion system, data acquisition system, battery module, and PC terminal.

The comprehensive experimental procedure is outlined as follows:

(1) Initial preparation: The peristaltic pump is deactivated, and the lithium battery module is positioned in a 25°C constant temperature chamber, maintaining the lithium battery in a stationary condition for a minimum of 6 hours. The coolant is maintained in a water bath at a constant temperature of 25°C.

(2) Commencement of the experiment: The peristaltic pump circulates the coolant within the loop. The coolant circulates into the battery module cooling plate within the constant temperature water tank, extracting heat from the battery. Upon cooling the battery module, the coolant circulates back to the constant temperature water tank through the loop, so concluding one cycle.

(3) Data recording: Temperature sensors are affixed to the lithium battery's surface and the cooling plate, transmitting real-time data to the PC through temperature transmitters. The positive and negative electrodes of the lithium battery are linked to a charge-discharge tester, which is operated by a computer. Throughout this interval, the data collecting system captures real-time temperature readings.

(4) Reiterate the aforementioned steps thrice. The final temperature is derived by averaging the outcomes of the three tests.

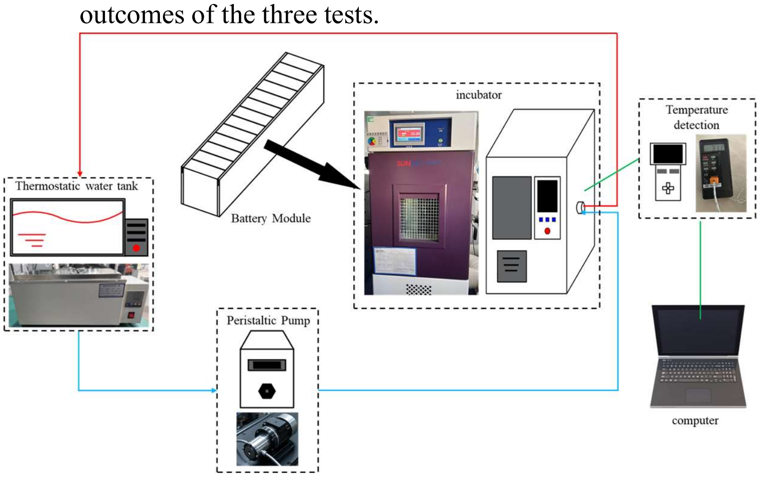

Fig.3. Experimental schematic representation

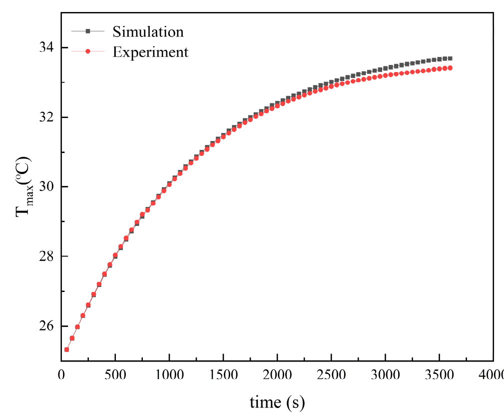

Fig.4. Comparison between modeling and experimental results

3.2 Results of Experiments

The numerical simulation's accuracy was corroborated by experimentation. Fig. 4 illustrates the comparison of T_{max} variations over time between simulated and experimental results. At the end of the experiment, △T was only 0.28°C. Referring to the study by Guo et al. [22], the experimental and simulation errors are considered acceptable. The experimental values are marginally lower than the modelling data, potentially attributable to heat source leakage during the experiment.

4 Comparative Analysis

4.1 Effect of Coolant Inlet Temperature on Cooling Performance

This section examines the influence of T_{in} on cooling performance. The influence of T_{in} on the cooling efficacy of the battery module is consistent and unaffected by the configuration of the cooling plate.

Consequently, this section selects a singular model (A-2) for comparative analysis. The battery module's initial temperature is established at 25℃, and the T_{in} of 21℃, 23℃, 25℃, 27℃, and 29℃ are examined. m_{in} is established at 3L/min, while all other initial and boundary parameters remain constant. Fig.5 illustrates the fluctuations in T_{max}, T_{min}, and $\varDelta T$ of the battery at various T_{in}.

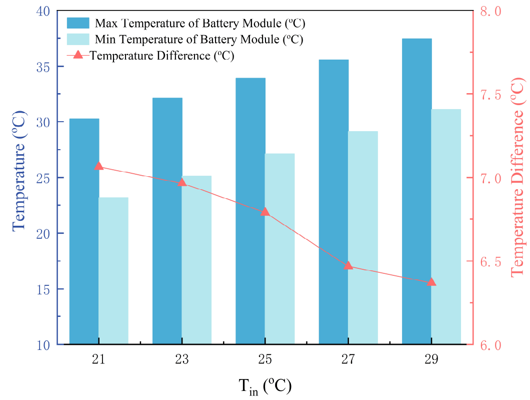

Fig.5. The influence of T_{in} on T and △T.

Fig.5 illustrates that when T_{in} escalates, both T_{max} and T_{min} of the battery grow, while △T diminishes. When T_{in} is below 25℃, the battery's T_{min} below 25℃, which is lower than its initial temperature. At this point, it may adversely affect the battery's performance and lifespan. From the standpoint of energy conservation and practical use, this is impractical; thus, T_{in} must not go below 25℃. When T_{in} exceeds 25℃, △T at T_{in} of 27℃ and 29℃ diminishes by 1.2% and 2.4%, respectively, in comparison to △T at 25℃. Nonetheless, the peak battery temperature rises by 6% and 11.5%, respectively. T_{in} exceeding the battery's initial temperature causes initial heating of the battery, with the cooling plates commencing heat dissipation only when the battery temperature surpasses T_{in}. This does not comply with the operational specifications of the cooling plate. The T_{in} must correspond to the battery's initial temperature. Consequently, future research will employ a coolant temperature of 25℃.

4.2 Impact of Structure on Cooling Performance

Thermal simulations were performed on the initial models of two types of cooling plates under the specified boundary conditions. Fig. 1(c) shows the initial flow channel configuration. Fig. 6 shows the T_{max}, T_{min}, and △T of the battery module under the initial flow channel configuration. The initial flow channel configuration ensures that the T_{max} of the battery module is below 40℃, indicating that the design of the initial model is reasonable. Fig. 6 shows that the A-1 model has a higher T_{min}, which is due to its larger flow channel spacing, leading to insufficient coolant flow in the corners, resulting in dead zones and localized overheating. The D-1 model, with a "semi-circular" design, fails to uniformly cover the battery module, causing significant △T between the batteries. The B-1 and C-1 models have the same coverage area but differ in coolant flow paths, leading to similar cooling performance. The E-1 and F-1 models uniformly cover the battery module, achieving similar cooling efficiency. Therefore, it can be concluded that the coverage method of the flow channels directly affects the heat dissipation performance of the cooling plate.

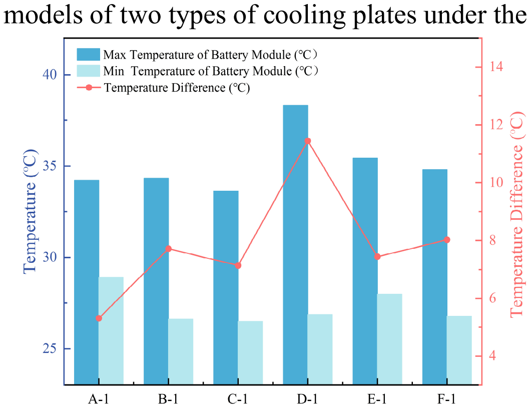

Fig.6. Comparative analysis of heat dissipation performance of six initial models

Next, optimization designs will be carried out for three model structures.

4.3 Optimization Design

The initial and optimized flow channel configurations are shown in Fig. 7, with comparative results for various structures presented in Figs. 8 and 9. Analysis of the two figures reveals that an increase in the number of flow channels enhances the cooling efficiency of the battery module. Augmenting the quantity of flow channels guarantees that the coolant encompasses all regions of the cooling plate, facilitating uniform heat absorption and dissipation. The B model features the widest spacing of flow channels. Dead zones persist in the B-3 model cooling plate, leading to inferior temperature regulation relative to the other two models, rendering it worthless of additional improvement. The A and C models have identical flow channel spacing, although their coolant flow courses diverge. The A-3 model's T_{max} is 33.595°C, which is 0.594°C less than that of the C-3 model. The A-3 model's T_{min} is 26.850°C, which is 0.237°C greater than that of the C-3 model, leading to more consistent battery temperatures in the A-3 model. The coolant in the A model traverses a greater distance, facilitating extended contact with the battery module and enhancing its heat removal capacity relative to the C model, thereby resulting in superior cooling performance.

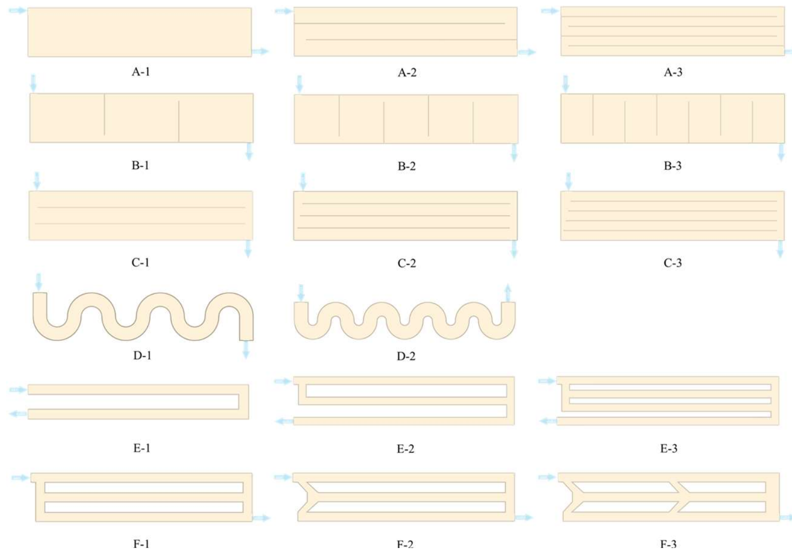

Fig.7. Optimization structure diagram of cooling plate

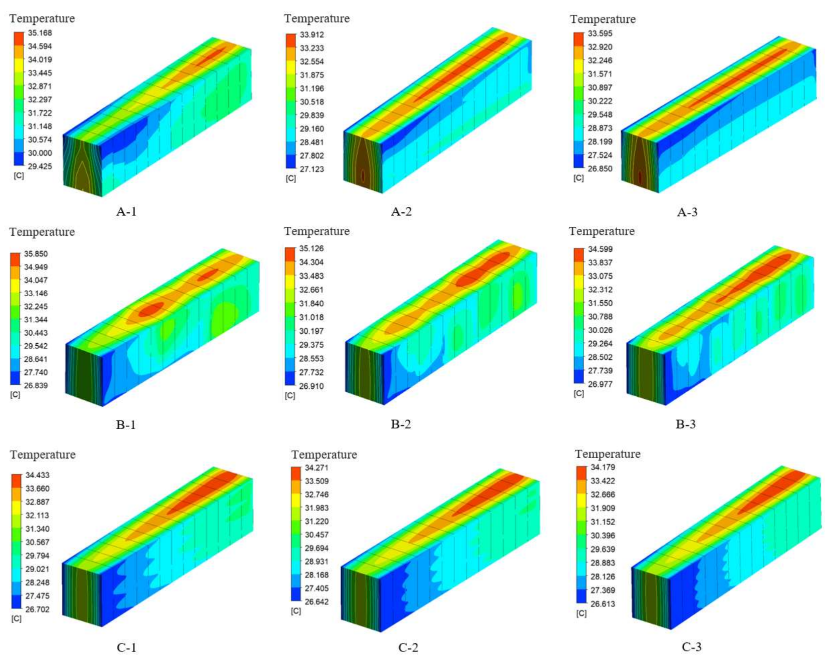

Fig.8. Temperature contour maps of nine types of ECP

Consequently, it can be inferred that the methodical design of flow channel quantity, optimization of channel widths, and modification of coolant flow distance over the cooling plate will substantially improve the cooling efficacy of the BTMS.

In the MCP, the quantity of semi-circles in the D-1 model was augmented to enhance the coverage area of the cooling plate, leading to the optimal D-2 model. Fig.9 illustrates that the cooling performance of the optimized model is subpar, even inferior to the initial E and F models. Consequently, this model was omitted from additional optimization. The E-1 model's flow channels were augmented, leading to the development of the E-2 and E-3 versions. Fig.9 illustrates that T_{max} of the E-2 and E-3 models is 34.983°C and 34.072°C, respectively, indicating substantial decreases relative to the E-1 model. T_{max} is situated at the center of the battery module's rear, whilst the cooling plates are positioned along the sides. This phenomenon cannot be modified by altering the configuration of the cooling plates. The examination of the F-1 model indicated that the flow capacity of the center micro-channels is subpar com-pared to that of the upper and lower microchannels. The F-2 and F-3 models were refined according to this discovery. Fig.9 clearly demonstrates that the temperature decrease is negligible, merely 0.1°C. This results from the battery's restricted thermal conductivity. Despite enhanced flow capacity in the central channels, the temperatures at both the top and bottom of the battery module remain inadequately mitigated, diminishing the value of the optimization.

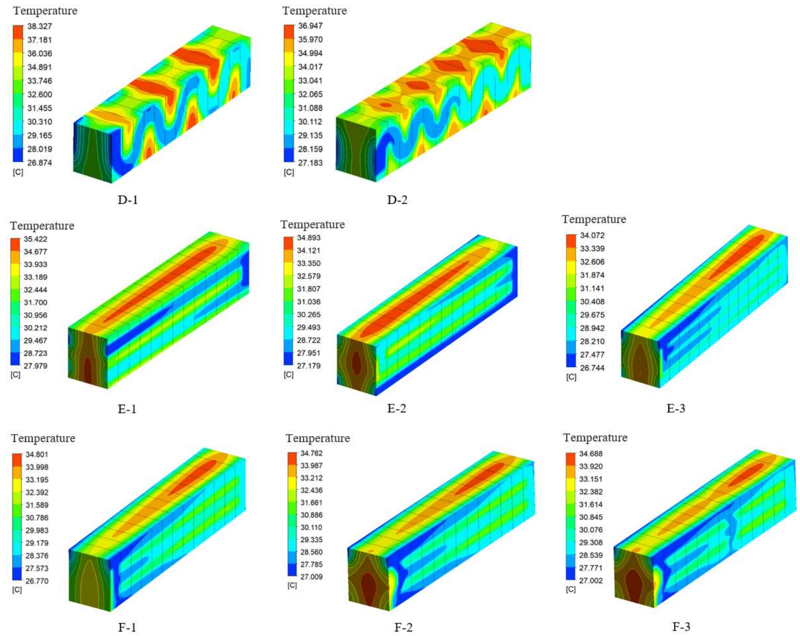

Fig.9. Temperature contour maps of eight types of MCP

Optimization examination of the three models revealed that, under the initial conditions, the E-3 model had superior cooling performance post-optimization.

4.4 The Effect of Mass Flow Rate on Cooling Performance

The mass flow rate (m_{in}) was designed with five different values, with all other boundary conditions remaining constant, for simulation analysis. Fig.10 illustrates a comparison of the cooling efficacy of several cooling plate configurations at varying m_{in}. As m_{in} increases, T_{max} of all models corres-pondingly lowers.

For the entire cooling plate, when m_{in} reaches 3L/min, the T_{max} and T_{min} of the battery stabilize with further increases in m_{in}. With the exception of the A-1, B-2, and B-3 models, T_{max} in all other configurations to remain below 35°C. Nonetheless, △T within the battery gra-

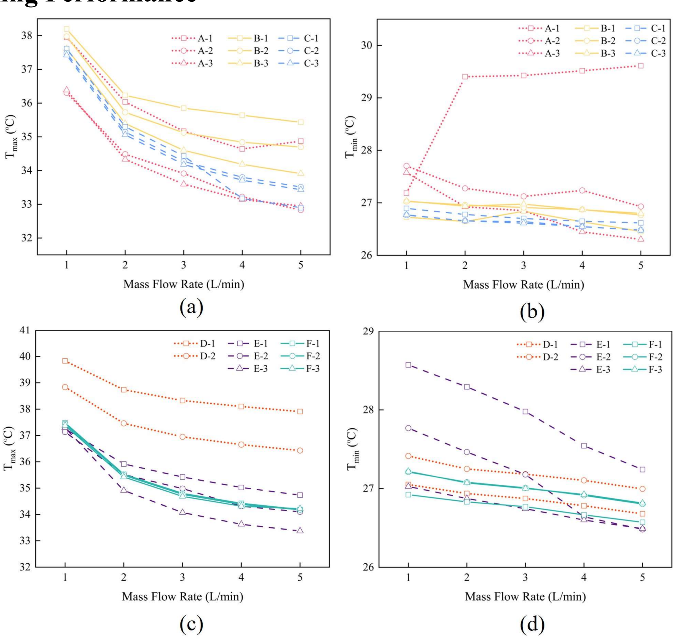

Fig.10. (a) Relationship between the *Tmax* of ECP and m_{in} (b) Relationship between the *Tmin* of ECP and m_{in} (c) Relationship between *Tmax* of MCP and m_{in} (d) Relationship between *Tmin* of MCP and m_{in}

dually increases as the flow rate rises. This is mostly because to the restricted thermal conductivity of the battery pack, which hinders the rapid passage of interior temperatures to the sides, leading to a reduction in heat exchange efficiency with the coolant.

In the A-1 model, no flow channels were incorporated, and when m_{in} escalated from 1L/min to 2L/min, T_{min} increased from 27.186°C to 29.404°C. The reduction of coolant in the lower-left and upper-right corners of the cooling plate increased the dead zones, resulting in an elevation of T_{min} of the battery module. Fig.10(a) illustrates that T_{max} of the two optimized models, A-2 and A-3, are inferior to those of the other models. In Fig.10(b), the A-2 and A-3 models exhibit higher T_{min} than the other models, leading to improved regulation of temperature disparities across the battery modules in these models. The analysis reveals that of the optimized models, the A-3 model exhibits superior temperature regulation, fulfilling the operational criteria.

The coolant in the microchannel cooling plate is dispersed more consistently than over the whole cooling plate, leading to a reduction in dead zones. At m_{in} of 1L/min, the flow velocity is insufficient, preventing the coolant from adequately dissipating heat, resulting in elevated temperatures in both the battery module and the cooling plate. Nonetheless, as m_{in} escalates to 2L/min, the temperature in the E and F models markedly declines. The peak temperature of the battery module decreases by 1.6°C in the E-2 model, 2.381°C in the E-3 model, and 1.9°C in both the F-2 and F-3 versions. The microchannel cooling plate exhibits effective cooling capability at low flow rates. From Fig.10(c) and Fig.10(d), it can be observed that T_{max} and T_{min} of the E-3 model are lower than those of the other models, indicating the best cooling performance. This satisfies the operational requirements.

4.5 Comprehensive comparison

In the design of cooling plates for power batteries, the convective heat transfer coefficient (h_c) and Nusselt number (Nu) play a crucial role. The calculation of these two parameters helps evaluate and optimize the thermal management capability of the cooling system, ensuring that the battery operates within an appropriate temperature range during charging and discharging processes, thus preventing performance degradation or safety issues due to overheating. The h_c and Nu can be calculated using the following equations: [23]

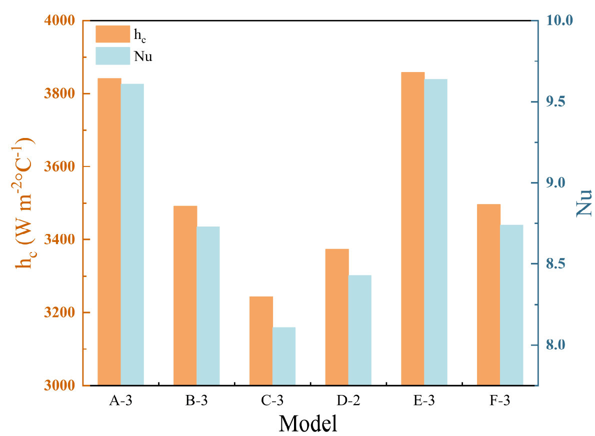

Fig.11. Comparison of h_c and Nu with six optimal cooling plate structures

$$h_c = \frac{m_{in} c_{p,l} (T_{out} - T_{in})}{A_c \left[T_{avg,w} - (T_{out} + T_{in})/2 \right]} \tag{12}$$

$$Nu = \frac{h_c d}{k_l} \tag{13}$$

In the equation, A_c represents the wetted surface area of the cooling plate, T_{out} is the outlet temperature of the coolant, and $T_{avg,w}$ is the average temperature of the inner wall in contact with the fluid.

Fig.11 displays the hc and Nu for six optimal cooling plate structures. When m_{in} is 3L/min, the h_c

and Nu of A-3 and E-3 are similar, indicating that their heat dissipation performance is comparable, which is also supported by the cloud plot. Additionally, their Nu values outperform the cooling plates designed by SenZhan et al. The other four cooling plate designs result in localized high temperatures within the battery module, leading to slightly lower h_c and Nu values. This validates the previous thermal performance analysis.

5 Conclusion

A thermal management model for the lithium battery module was developed and experimentally verified. The influence of parameters including inlet coolant temperature, channel configuration, number of channels, and inlet mass flow rate of the cooling plate on the thermal properties of the battery module was examined. A thorough comparison of the cooling performance between ECP and MCP structure was performed. The subsequent conclusions were derived:

1. The impact of varying the inlet coolant temperature on cooling performance was investigated. Given the prevailing operating conditions, the inlet coolant temperature was finally engineered to align with the ambient temperature.

2. This work involved the creation and subsequent optimization of six types of cooling plates. It was determined that the flow channels of ECP must be meticulously designed to minimize dead zones and enhance the coolant flow distance. For MCP, the distribution of flow channels must be tuned to attain cooling performance equivalent to that of ECP, despite reduced coverage areas.

3. A comprehensive comparison of the best models from both ECP and MCP was conducted. The convective heat transfer coefficient (h_c) and Nusselt number (Nu) were calculated, revealing that the optimized A-3 and E-3 models exhibit similar cooling performance.

The study presented in this paper demonstrates that MCP allows for more flexible flow channel design, effectively preventing localized overheating. Aligned with lightweight design principles, it reduces material usage while maintaining thermal performance, thereby decreasing weight. Due to its efficient heat dissipation capabilities, the required coolant volume is lower, further reducing the overall weight of the cooling system. Therefore, considering cost and future optimization requirements, MCP is a viable option for the design of thermal management systems for lithium-ion batteries.

Acknowledgment

This work is financially supported by Qing Lan project of the Higher Education Institutions of Jiangsu Province and Science, Technology Plan Project of Jiangsu Province (International Science and Technology Cooperation Special Fund) (BZ2022029) and Jiangsu Keyi New Energy Technology CO., LTD.

References

[1] Hannan, M.A., *et al*., Review of energy storage systems for electric vehicle applications: Issues and challenges. *Renewable and Sustainable Energy Reviews*, 69 (2017), pp.771-789.

[2] Yang, Y., *et al*., Battery energy storage system size determination in renewable energy systems: A review. *Renewable and Sustainable Energy Reviews*, 91 (2020), pp.109-118.

[3] Wang, Q., *et al*., A critical review of thermal management models and solutions of lithium-ion batteries for the development of pure electric vehicles. *Renewable and Sustainable Energy Reviews*, 64 (2018), pp.106-128.

[4] Sun, Y., *et al*., Safety issues and mechanisms of lithium-ion battery cell upon mechanical abusive loading: A review. *Energy Storage Materials*, 34 (2021), pp.181-206.

[5] L. Y. Zhao, *et al*., A novel thermal management system for lithium-ion battery modules combining direct liquid cooling with forced air-cooling, *Applied Thermal Engineering*, 232 (2023) 120992.

[6] Guo, Y., *et al*., Modeling and analysis of liquid-cooling thermal management of an in-house devel oped 100 kW/500 kWh energy storage container consisting of lithium-ion batteries retired from e lectric vehicles. *Applied Thermal Engineering*, 232 (2023) 121111.

[7] Song, L., *et al*., A comprehensive investigation of thermal runaway critical temperature and ener gy for lithium iron phosphate batteries. *Journal of Energy Storage*, 86 (2024) 111162

[8] Lin, H., *et al*., Thermal Modeling Considering Anisotropy of the 280Ah Lithium Iron Phosphate Battery. *International Conference on Electrical Machines and Systems*, 2023, pp. 2187-2192

[9] Li, W., *et al*., A Comparative Numerical Study of Lithium-Ion Batteries with Air-Cooling System s towards Thermal Safety. *Fire*, 7 (2024) 29.

[10] Y. Zhang., *et al*., Effects of one special-shaped pin fin on the flow and heat transfer performance i n the liquid cooling plate for a battery pack, *International Journal of Thermal Sciences*, 195 (202 4) 108643.

[11] C. Z. Hu., *et al*., Experimental and numerical investigations of lithium-ion battery thermal manag ement using flat heat pipe and phase change material, *Journal of Energy Storage*, 55 (2022) 1057 43.

[12] L.K. Singh., *et al*., A numerical study on thermal management of a lithium-ion battery module via forced-convective air- 28 cooling, *International Journal of Refrigeration* 131 (2021) 218-234,

[13] G. Zhao., *et al*., A review of air-cooling battery thermal management systems for electric and hyb rid electric vehicles, *Journal of Power Sources* 501 (2021) 230001.

[14] H.F. Fang., *et al*., Comparative analysis of cooling effect of battery module cooling plate structur es, *Thermal Science* 00 (2023) 166-166.

[15] S. Lin., *et al*., Thermal performance of rectangular serpentine mini-channel cooling system on lith ium battery, *Journal of Cleaner Production*, 418 (2023) 138125.

[16] Y.S. Zhang., *et al*., Comparative study on the performance of different thermal management for e nergy storage lithium battery, *Journal of Energy Storage*, 85 (2024) 111028.

[17] J.K. Xie., *et al*., A novel strategy to optimize the liquid cooling plates for battery thermal manage ment by precisely tailoring the internal structure of the flow channels, *International Journal of Th ermal Sciences*, 184 (2023) 107877.

[18] K. J. Li., *et al*., Multi-objective optimization of side plates in a large format battery module to mit igate thermal runaway propagation, *International Journal of Heat and Mass Transfer*, 186 (2022) 122395.

[19] J.C. Xu., *et al*., Simulation research on thermal management system of battery module with fin he at dissipation structure, *Applied Thermal Engineering*, 239 (2024) 122177.

[20] Z.Y. Zou., *et al*., Numerical study on a novel thermal management system coupling immersion co oling with cooling tubes for power battery modules, *Journal of Energy Storage*, 83 (2024)110634

[21] Wang, S., *et al*., Experimental study of gas production and flame behavior induced by the thermal runaway of 280 Ah lithium iron phosphate battery, *Journal of Energy Storage*, 74 (2023) 109368.

[22] R. Guo., *et al*., Heat dissipation analysis and optimization of lithium-ion batteries with a novel pa rallel-spiral serpentine channel liquid cooling plate, *International Journal of Heat and Mass Tran sfer*, 189 (2022) 122706

[23] S, Zhan et al., Topology optimization of liquid cooling plate for lithium battery heat dissipation b ased on a bionic leaf-vein structure, *International Journal of Heat and Mass Transfer*, 231 (2024) 125898

Received: 29.12.2024.
Revised: 10.04.2025.
Accepted: 14.04.2025.